

Article

A Convolutional Neural Network for the Removal of Simultaneous Ocular and Myogenic Artifacts from EEG Signals

Maryam Azhar , Tamoor Shafique *  and Anas Amjad 

School of Digital, Technology, Innovation and Business, University of Staffordshire, Stoke-on-Trent ST4 2DE, UK; maryam.azhar@staffs.ac.uk (M.A.); a.amjad@staffs.ac.uk (A.A.)

* Correspondence: tamoor.shafique@staffs.ac.uk

Abstract: Electroencephalography (EEG) is a non-invasive technique widely used in neuroscience to diagnose neural disorders and analyse brain activity. However, ocular and myogenic artifacts from eye movements and facial muscle activity often contaminate EEG signals, compromising signal analysis accuracy. While deep learning models are a popular choice for denoising EEG signals, most focus on removing either ocular or myogenic artifacts independently. This paper introduces a novel EEG denoising model capable of handling the simultaneous occurrence of both artifacts. The model uses convolutional layers to extract spatial features and a fully connected layer to reconstruct clean signals from learned features. The model integrates the Adam optimiser, average pooling, and ReLU activation to effectively capture and restore clean EEG signals. It demonstrates superior performance, achieving low training and validation losses with a significantly reduced *RRMSE* value of 0.35 in both the temporal and spectral domains. A high cross-correlation coefficient of 0.94 with ground-truth EEG signals confirms the model's fidelity. Compared to the existing architectures and models (FPN, UNet, MCGUNet, LinkNet, MultiResUNet3+, Simple CNN, Complex CNN) across a range of signal-to-noise ratio values, the model shows superior performance for artifact removal. It also mitigates overfitting, underscoring its robustness in artifact suppression.

Keywords: electroencephalography (EEG); EEG denoising; artifact removal; convolutional neural network (CNN); deep learning (DL)



Citation: Azhar, M.; Shafique, T.; Amjad, A. A Convolutional Neural Network for the Removal of Simultaneous Ocular and Myogenic Artifacts from EEG Signals. *Electronics* **2024**, *13*, 4576. <https://doi.org/10.3390/electronics13224576>

Academic Editor: Jichai Jeong

Received: 2 October 2024

Revised: 17 November 2024

Accepted: 19 November 2024

Published: 20 November 2024



Copyright: © 2024 by the authors. Licensee MDPI, Basel, Switzerland. This article is an open access article distributed under the terms and conditions of the Creative Commons Attribution (CC BY) license (<https://creativecommons.org/licenses/by/4.0/>).

1. Introduction

Healthcare has been significantly revolutionised with the emergence of artificial intelligence, machine learning, and deep learning. Machine learning and deep learning algorithms have been employed to address several challenges. Deep learning and machine learning have advanced detection, diagnosis, and treatment across various medical conditions. Significant progress has been made in cancer detection [1–3], pathological analysis [4], cardiac health issues [5,6], neurological analysis [7,8], and in developing surgical innovations and training systems, including robotic surgical systems [9] and surgical skill assessments [10].

Electroencephalography, commonly known as EEG, is a measure of the electrical activity generated by the brain. The electrical activity is generated by the neuron's synapses in the cerebral cortex of the brain. These electrical impulses are produced due to the synchronised activity of the neurons depending on the state of consciousness along with mental and emotional functions [11,12]. Emotion recognition [13], identification of different brain activities [14], and pathology analysis [15] are prominent applications of EEG.

EEG is a non-invasive method used to monitor the brain's electrical activity by placing multiple electrodes on the scalp to detect and record the electrical impulses generated by the brain. The quality of the EEG is often distorted by several factors, including noise from the electrodes and physiological artifacts like ocular and myogenic artifacts. Myogenic artifacts originate from the activity of the frontalis and temporalis muscles, while eye movement

and eye blinks give rise to ocular artifacts. Eye movement creates a sudden change in the resting potential of the retina. This change in the potential is captured by the electrodes and appears as sharp spikes in the EEG signals which spread rapidly through the neural activity detected by the electrodes. Meanwhile, blinks are more pronounced and show up as slow and large voltage changes [16]. Muscular artifacts can be recorded all over the scalp, and the extent of the disturbance depends on the movement of different muscles like the jaw, neck, or face [17], or the changes caused by breathing and sweat-induced electrodermal interference. These artifacts appear as sharp changes in EEG signal amplitude, which mimic brain activity and are often misinterpreted as brain activity. As depicted in Figure 1 [18], the resting EEG signals are shown at the top while the EEG signals containing artifacts originating from eye movement and eye blinks are shown in Figures 1a and 1b, respectively, while Figure 1c depicts how heavily EEG signals are corrupted when there is muscle tension in the area surrounding the electrodes. This misinterpretation of EEG signals increases the need to detect and remove artifacts by processing contaminated EEG signals.

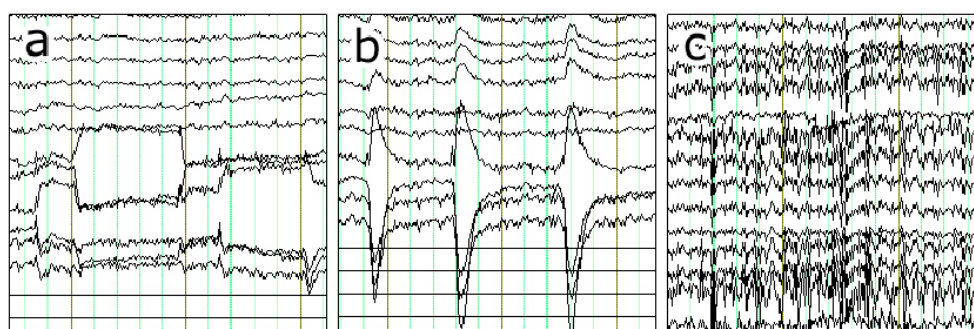


Figure 1. Artifacts in EEG: (a) eye movement, (b) eye blinks, and (c) muscle tension [18].

To remove these artifacts, several techniques have been developed so far. Some of the techniques that are widely used employ independent component analysis (ICA) [19], wavelet transform [20], and adaptive filters [21]. Although these methods have been used widely, they require expert observation for identifying the artifacts as well as significant loss alongside artifact removal. Due to these reasons, deep learning-based models have become significant tools to perform the task of artifact removal. Several studies have presented models for artifact removal such as a U-net-based model [22] for EOG artifact removal which made use of U-net [23], a model commonly used for image segmentation. Another study [24] presented four benchmark networks for artifact removal along with a benchmark EEG dataset to be utilised in further studies. These studies have been successful in removing artifacts from EEG signals. However, these techniques are generally effective at removing either ocular artifacts or myogenic artifacts but not both simultaneously.

Existing artifact removal techniques often eliminate clean EEG signals along with ocular and myogenic artifacts from the contaminated EEG data, which reduces the accuracy of the resulting signal. Moreover, existing denoising models are particularly effective only when addressing a single type of artifact; however, they struggle to maintain accuracy when dealing with multiple types of artifacts due to the increased complexity within the EEG signals. This limitation largely stems from unsuitable model parameters, making existing models inefficient for simultaneously removing multiple artifacts.

This paper presents a novel deep learning framework explicitly designed to significantly advance the accuracy of EEG signal analysis by addressing the simultaneous removal of ocular and myogenic artifacts. The proposed model employs a sophisticated architecture combining convolutional layers with a fully connected layer, further optimised using the ReLU activation function. A distinguishing feature of this approach lies in its ability to minimise information loss during the artifact removal process, which is critical for preserving the integrity of the original EEG signals. Additionally, the model's performance is further

refined using the Adam optimiser, accompanied by the meticulous fine-tuning of network parameters, ensuring optimal convergence and artifact suppression.

The remainder of this paper is structured as follows: Section 2 is a literature review of existing conventional and deep learning-based models used for denoising and removing different artifacts from EEG signals. Section 3 investigates the dataset used and the network structure of the neural network. The processes and parameters for training the neural network are also discussed in this chapter. Section 4 presents and discusses the results obtained from training and evaluating the neural network. Finally, Section 5 presents the conclusions drawn from the research, outlines the limitations of the proposed work, and identifies directions for future research.

2. Literature Review

The presence of unwanted components in EEG results in inaccurate and erroneous analysis. To remove these artifacts efficiently, different denoising methods have been developed over the years. This review explores both conventional denoising techniques and deep learning-based approaches to provide an overview of their effectiveness in EEG artifact removal.

2.1. Conventional Methods for Artifact Removal

Independent component analysis (ICA) is used to remove the components which differ from the original EEG signal and to generate noise-free EEG signals [25]. ICA-based software EEGLab v7.1.7.18b [26] was also employed in research [19] to detect and remove the artifacts present in EEG signals. Although effective, it removes the clean EEG signals as well as the noisy signals without any manual check. Another study [21] was also successful in removing artifacts from EEG signals while reducing the loss of information by making use of ICA, multivariate empirical mode decomposition (MEMD), and factor analysis (FA).

Another study [27] employed both ICA and regression in combination to break the signal components in independent components and to identify the noisy components. The noisy components were then removed by linear regression. This method was highly effective at removing the artifacts but failed to preserve clean EEG signals, as components of clean EEG signals were also removed. To rectify this loss of EEG signals, a moving average filter (MA) smoothed the signal by replacing each data value with the average neighbouring values after ICA to preserve the signals.

Wavelet transform has also been widely used to discard the artifacts present in EEG signals. A past study [28] detected and removed the wavelets containing artifacts and utilised the remaining wavelets to reconstruct a clean EEG signal. This resulted in an inaccurate reconstruction of the denoised EEG signal when used on its own. When it is used with ICA [29], ICA separates the artifacts from the EEG signals while discrete wavelet transform removes these artifacts and reconstructs a clean EEG signal. The main limitation of using wavelet transform turns out to be the inaccurate reconstruction of the denoised EEG signal and mistakenly eliminating parts of the clean EEG signal along with the artifacts.

In addition to wavelet transform and ICA-based methods, EEG denoising is also performed by using other signal processing techniques such as filters, including adaptive filters [30], the Kalman filter [31], and the Wiener filter [32]. High-pass filters [33] and band-pass filters [34] are also capable of rejecting certain frequencies relating to artifacts present in the EEG signal. Though effective, there is a risk of removing the frequency components of the EEG signal along with the artifacts which can result in data loss. Other methods include variational mode decomposition [35], empirical mode decomposition [36,37], and canonical correlation analysis (CCA) [38]. These EEG-denoising techniques rely on linear transformation and assumptions which can result in data loss during the analysis and reconstruction of the EEG signals. CCA-based methods for removing EMG artifacts determine the artifact and then decompose it into multiple uncorrelated components [38], assuming a low autocorrelation between the artifacts. CCA has also been used along with

Ensemble EMD (EEMD) to remove artifacts from EEG signals [39] where the values of autocorrelation are chosen by trial and error. Because of the dependency of these methods on presumptions, these methods are unreliable even though they have shown effective performance in removing artifacts from contaminated EEG signals.

2.2. Deep Learning-Based Methods for Artifact Removal

Deep learning approaches to EEG denoising allow a focus towards data-driven algorithms for artifact removal, which has been made possible due to the availability of data-rich datasets. Deep learning-based models are also capable of removing EEG artifacts in an integrated manner to capture dependencies and perform optimisation for artifact removal throughout processing.

EEG reconstruction [40] and EEG data augmentation [41] are the most noticeable examples of EEG-related analysis techniques. Several deep learning-based models have been implemented and utilised to remove artifacts from EEG signals. Some of them are GANs [42], recurrent neural networks (RNNs) [43,44], Simple and Complex CNNs [45], and auto encoders [46]. Four benchmark networks have also been presented [24] for ocular and myogenic artifacts individually along with a benchmark EEG dataset. Although effective, the networks behave poorly on low noise levels. Even though deep learning-based models have made significant progress in the denoising of EEG signals and the removal of artifacts present in them, they still lack in terms of robustness, dataset, generalisability, and the artifacts removed. Based on these drawbacks, there is a need to make improvements in the existing models and to develop the appropriate performance metrics to evaluate EEG-denoising models.

3. Methodology

3.1. Problem Definition

Ocular and myogenic artifacts corrupt the EEG signal while EEG is being performed on a patient. The artifacts are independent of clean EEG signals and are called background noise. The individual impact of ocular and myogenic artifacts on clean EEG signals is expressed in Equation (1).

$$Y = X + \lambda \times (A_O + A_M) \quad (1)$$

where Y , X , A_O , and A_M represent the noisy EEG signal, clean EEG signal, ocular artifact and myogenic artifacts, respectively, while λ represents the relative contribution of an artifact, which can be controlled with the value of the signal-to-noise ratio (SNR). Equation (2) expresses how the SNR is calculated.

$$SNR = 10 \log \frac{RMS(X)}{RMS(\lambda \times (A_O + A_M))} \quad (2)$$

EEG signals are denoised to remove the artifacts present in noisy EEG signals to estimate and predict clean EEG signals. The deep learning model learns the artifacts ' A_O ' and ' A_M ' present in the noisy EEG signal ' Y ' utilising the knowledge learned during the training process and filters out any artifacts present in the noisy EEG signal ' Y '.

The main aim of this paper is to effectively denoise noisy EEG signals using the proposed model to remove the simultaneously occurring ocular and myogenic artifacts present in noisy EEG signals. The model is implemented to remove the ocular and myogenic artifacts present in the noisy EEG signals by optimising the existing model [43]. The model's performance is optimised using the Adam optimiser to adaptively adjust learning rates, enhancing the training process and fine-tuning the network parameters while extending the training and validation processes to achieve faster convergence and lower losses. This also results in the increased accuracy of the denoising model [43] and expands its capability to remove various types of artifacts. Figure 2 depicts the proposed framework for the simultaneous EOG-EMG artifact removal.

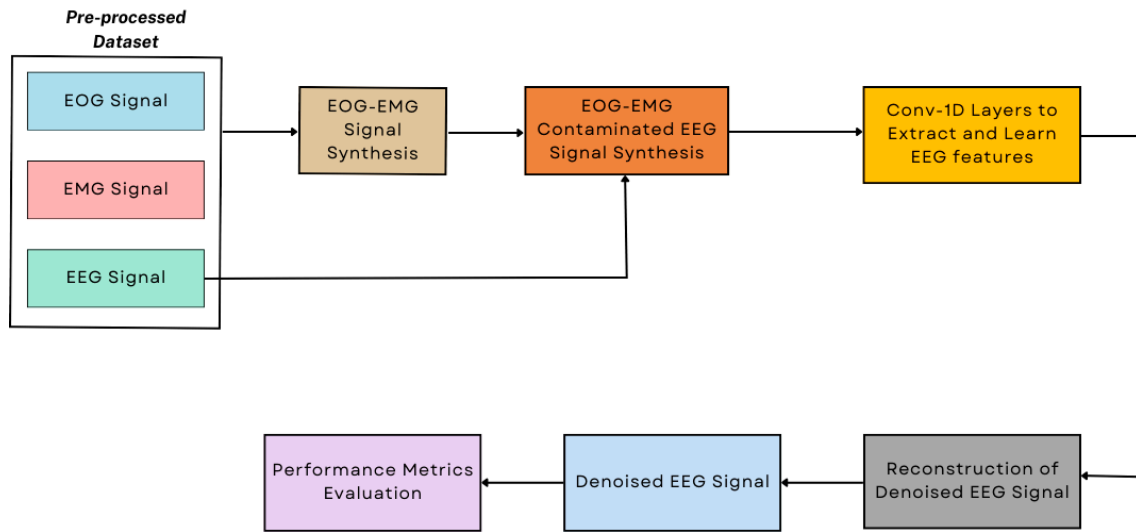


Figure 2. Framework for simultaneous EOG-EMG artifact removal.

3.2. Dataset

The dataset used in this paper for training and testing purposes was EEGdenoiseNet [24]. EEGdenoiseNet was developed for the purpose of training and testing denoising models based on deep learning and is already pre-processed. The dataset contains 4514 clean EEG signals, 3400 EOG (Electrooculogram) signals, and 5598 EMG (Electromyograph) signals. The noisy EEG segments were produced by introducing noise using EOG and EMG signals into the clean EEG signals, which were taken as the ground-truth clean EEG signals.

3.3. Generation of Contaminated EEG Signals

The ground-truth and the noisy EEG signals were generated using the EOG, EMG, and EEG signals from the EEGdenoiseNet dataset for training and testing purposes. As the artifacts were introduced in the EEG signals linearly, the EOG and EMG segments were added into the clean EEG signals from the dataset to generate the noisy EEG signals, as shown in Figure 3.

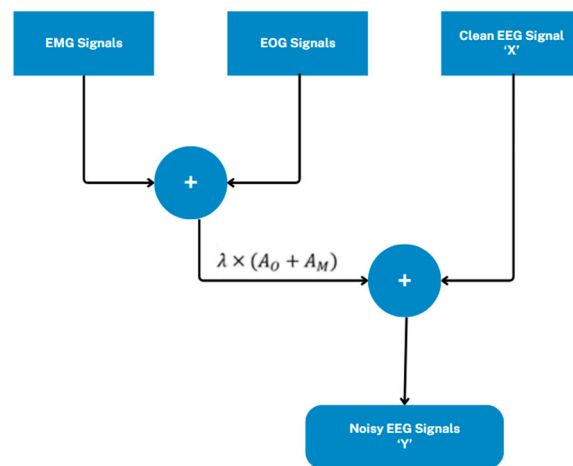


Figure 3. Noisy EEG signal synthesis.

Figure 4 displays a comparison of the clean EEG signal and the contaminated EEG signal. The clean EEG signals and the noisy EEG signals were used to train and validate the model.

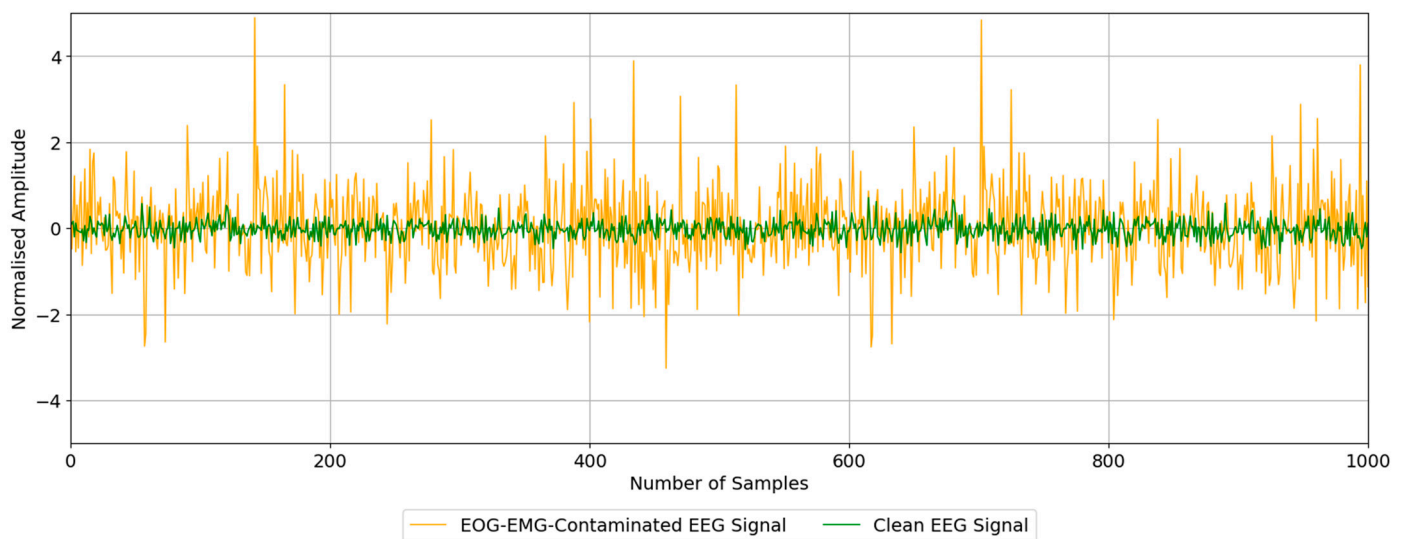


Figure 4. Example segment of simultaneous EOG- and EMG-corrupted EEG signal and ground-truth EEG signal.

As the simultaneous EOG-EMG-contaminated EEG signals were obtained by the random and uncorrelated addition of the artifacts into the clean EEG signals, this provided a controlled baseline for various models' generalisability without dealing with the more complex nature of locked EOG-EMG signals which depends on the high correlation of both artifacts. This approach also provides a wide range of signal–noise profiles and helps prevent generalisability on extremely specific artifact trends.

To synthesise the noisy EEG signals containing both artifacts, the 5598 EMG segments were randomly added to 3400 EOG segments. Some of the EOG segments were reused so that the dimensions of the EOG and EMG segments are the same, as previously conducted in other studies [23,43,44] for adding only EMG segments into the EEG signals to generate EMG-corrupted EEG signals. The combined EOG-EMG artifact segments were added to the EEG signals by dropping some segments to match the dimensions of the clean EEG dataset, which was 4514, and by making use of the fact that the artifacts were linearly additive in nature. Before addition, the combined EOG-EMG artifact segments and clean EEG segments were shuffled and split into training, validation, and testing datasets, with 80% assigned for training, 10% for validation, and 10% for testing, by following the techniques outlined by the authors of EEGdenoiseNet [24] and existing studies [47,48].

To synthesise the noisy EEG signal, the segments from both sets were linearly combined with each other according to Equation (1), with signal-to-noise ratios ranging from -7dB to $+2\text{dB}$. To expand the size of the training, validation, and testing sets, the combined EOG-EMG segments and the clean EEG segments were linearly recombined ten times in a random manner, at an interval of one. The use of various *SNR* values across noisy EEG signals introduced diversity in the data for the model to better generalise and to avoid exposure to familiar noise patterns. As a result, the training set consisted of 36,110 pairs, while the validation set and the testing set consisted of 4520 and 4510 pairs, respectively.

3.4. Network Structure

The deep learning model for denoising the EEG signals was developed with seven 1-D convolutional blocks, each having two convolutional layers with the same number of filters followed by a ReLU function. The size of the filters increased exponentially from 32 to 2048 in each block with a kernel size of 3 and a stride of 1. The increase in filter size in each block increased the feature dimensions, enabling different numbers of features to be extracted in each layer. An average pooling layer with a size of 2 followed each convolutional block which reduced the spatial dimensions of the block output, but the number of channels

remained the same. The pooling layer was followed by a dropout layer with a rate of 0.5 to introduce randomness to the system to make it robust and avoid overfitting.

To make the output data compatible with the dimensions of the fully connected layer, a flatten layer was used after the last convolutional block. The two-dimensional output from the convolutional block was converted into a one-dimensional vector by stacking all the values in a single dimension. This enabled the flatten layer to lose the spatial dimension but retain its depth, which acted as the channel information and was input to the fully connected layer to reconstruct the EEG signal and produce a denoised EEG signal. In the fully connected layer, each neuron was connected to the subsequent neuron in the flatten layer, resulting in a reconstructed EEG signal which was the prediction required from the model and had the same dimensions as the input given to the model. The network structure for the model is displayed in Figure 5.

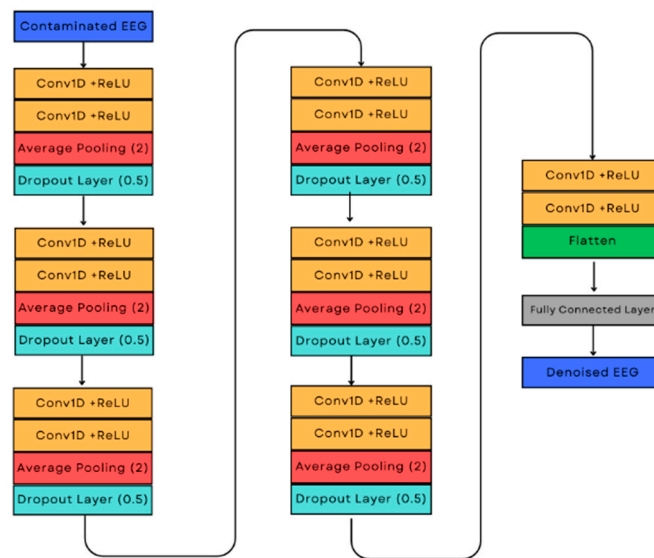


Figure 5. Network structure for the denoising model.

A detailed view of how the EEG signal dimensions change after every layer is shown in Figure 6. The number of channels or the width of the EEG signal in the output dimensions relate to the number of filters applied in the convolution layer while extracting the feature. The length of the EEG signal decreases exponentially as features are extracted.

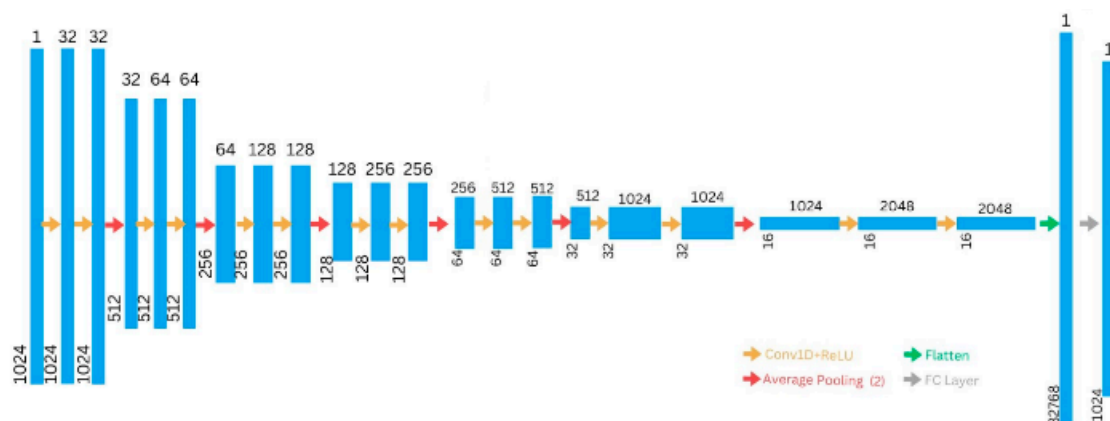


Figure 6. EEG signal dimensions in each layer.

3.5. Training and Validation

To overcome the problem of instability and slow convergence during training, the clean and noisy EEG signals were normalised. Normalising the clean and noisy EEG

signals scales the signals to a common range for time points, which maintains the relative relationship between the signals and avoids the potential overfitting of the model. The normalised signals can be represented by Equations (3) and (4).

$$\hat{X} = X/\sigma_Y \quad (3)$$

$$\hat{Y} = Y/\sigma_Y \quad (4)$$

where σ_Y is the standard deviation of the noisy EEG signal 'Y'. The normalised noisy EEG signal ' \hat{Y} ' is input to the neural network.

The neural network is defined as a non-linear function f that uses the samples from the noisy EEG signal distribution to map it to another distribution with respect to the learnable parameter θ , which is the estimation of the denoised EEG signal ' \tilde{X}_i ', with the difference between \hat{X}_i and \tilde{X}_i being minimised, as shown in Equation (5).

$$\tilde{X}_i = f(\hat{Y}_i, \theta) \quad (5)$$

The loss function of minimum square error (MSE) is used as a quality-of-service parameter to determine the accuracy of the predictions made by the model. It was used during the training and validation processes to reduce the difference between the clean and ground-truth EEG signals. The MSE determined the optimal weight parameters by making use of the stochastic gradient descent (SGD), which in turn used a random set of samples for noisy and clean EEG signals to update the training parameters, as shown in Equation (6).

$$L_{MSE} = \frac{1}{N} \sum_{i=1}^n \left(\hat{X}_i - \tilde{X}_i \right)^2 \quad (6)$$

where ' N ' is the total number of samples in an epoch while \hat{X}_i and \tilde{X}_i are the i th samples of the input normalised clean EEG signals and the denoised EEG signals, respectively.

The Adam optimiser was used during the training process to determine the optimal set of parameters to minimise the difference between the denoised and clean EEG signals. The Adam optimiser had the learning rate set as 0.0001 and the exponential decay rate for moment β_1 was set as 0.5, while the rate for β_2 was set as 0.9 with the value of epsilon ϵ set as 10^{-8} . The model was trained for 50 epochs with a batch size of 20 of randomly generated training datasets. The Adam optimiser was used for training as it can achieve a faster convergence because of the adaptivity of the learning rate according to the exponential decay for the first moment (mean) and second moment (uncentered variance), which helps the model to avoid overfitting. The learning rate was determined and adjusted according to the first and second moments. This adaptivity of the learning rate optimised the convergence of the network. The bias correction of the Adam optimiser also helped in estimating the moments more accurately for faster convergence. The Adam optimiser works more efficiently than the RMSprop optimiser because of the multiple moments as compared to the single moment in the RMSprop optimiser. By setting the value β_1 as 0.5, the network adapted faster to the changes in the gradients, while when β_2 was set as 0.9, more importance was given to the current gradients and less weight was given to the previous gradients. With RMSprop having only squared gradients (β) as opposed to the mean and squared gradients (β_1 and β_2) in the Adam optimiser, this gives past gradients more influence over the current gradient and slows down convergence. After training, the model was validated on an unseen dataset to determine the model performance and learning and to see if the model was overfitting. The model with the least validation loss was saved as the best-trained model and its weight parameters were used.

The proposed model was trained, validated, and tested 10 times along with Simple CNN and Complex CNN networks [24] to increase the statistical power of the results. The Simple CNN was made up of four 1-D convolutional layers with a filter size of 64 in each block along with a kernel size of 3 and stride of 1. Each convolutional layer was followed

by a batch normalisation layer along with an activation function of ReLU and dropout rate of 0.3. The Complex CNN stacked multiple residual blocks with kernel sizes of 3, 5, and 7 in three parallel branches with a 1-D convolutional layer at the beginning and at the end of the residual blocks. The Complex CNN used a dense layer at the end to produce the denoised EEG signals. All the networks were implemented in Python 3.10.12 in Google Colab with V100 GPU.

3.6. Evaluation

The trained model was then evaluated on a test dataset to observe the model's capability to generalise features across any unseen and new data. This evaluation was performed to ensure the model's robustness, reliability, and its applicability in a real-life setting where the model obtained new and unseen data as the input. The model denoised the unseen contaminated EEG signal, and the denoised EEG signal was evaluated by using three evaluation metrics: the relative root mean square error in the time domain $RRMSE(t)$, the relative root mean square error in the frequency domain $RRMSE(f)$, and the cross correlation (CC) between the input noisy signal and the denoised EEG signal obtained as the model's output.

The relative root mean square error in the time domain $RRMSE(t)$ (see Equation (7)) and the relative root mean square error in the frequency domain $RRMSE(f)$, (see Equation (8)) measure how well the denoised signal matches the properties of the input signal in time and frequency domain, respectively. A smaller value of both error functions displays a greater similarity between the signals.

$$RRMSE(t) = \frac{RMS(f(Y) - X)}{RMS(X)} \quad (7)$$

$$RRMSE(f) = \frac{RMS(PSD(f(Y)) - PSD(X))}{RMS(PSD(X))} \quad (8)$$

The cross correlation (CC) between the input noisy signal and the denoised EEG signal determines the similarity and alignment between both signals (see Equation (9)). A higher value of cross correlation indicates a high similarity between both signals.

$$CC = \frac{Cov(f(Y), X)}{\sqrt{Var(f(Y))Var(X)}} \quad (9)$$

Additionally, the quality of the denoised EEG signals was also evaluated by estimating the power ratios in all five frequency bands of EEG signals i.e., Delta (0.5–4 Hz), Theta (4–8 Hz), Alpha (8–13 Hz), Beta (13–30 Hz), and Gamma (30–80 Hz) [49], against the power of the EEG signal across the whole spectrum. The average power ratios were calculated for the clean EEG signal, noisy EEG signal, and denoised EEG signal. As the ocular artifacts and myogenic artifacts existed in the frequency ranges of 0.2–4 Hz and 20–100 Hz, respectively, the power ratio helped determine how well the denoised EEG signals related to the clean EEG signals in the spectral domain. For the closely related numerical value of the estimated power ratio for the denoised EEG signal and clean EEG signal in any frequency band, the predicted signal was more closely related to the ground-truth signal. On the contrary, the estimated power ratio for the noisy EEG signal and the clean EEG signal were expected to be numerically far apart. The power ratio for a frequency band was calculated by dividing the power of a frequency power band with the total power of the whole signal.

4. Results and Discussion

4.1. Training and Validation Losses

The mean square error (MSE) was calculated while training and validating the model's performance on the dataset. MSE was used as a quality-of-service parameter to determine the accuracy of the predictions made by the model. The proposed model was trained and validated using EEG signals which were contaminated with EOG and EMG artifacts

simultaneously. As depicted in Figure 7, the MSE decreased significantly as the model was trained, which indicates that the model effectively generalises the features of the artifacts it learns during training. The decrease in validation loss also indicates that the model avoids the problem of overfitting. As the gap between the loss values of training loss and the validation loss is small, this indicates that the model can learn and generalise meaningful features from the training data.

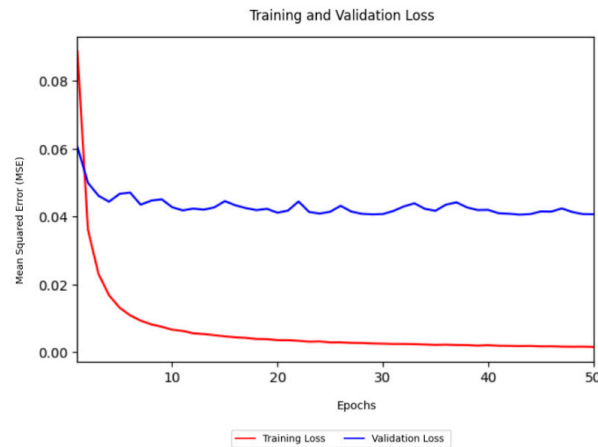


Figure 7. Training and validation loss curves for the proposed model.

4.2. Benchmark Networks

To observe the performance of the proposed model in comparison to the existing models, the Simple CNN and the Complex CNN were trained and tested on the same contaminated EEG with simultaneous myogenic and ocular artifacts. As shown in Figure 8, the validation loss of both the networks increases significantly while the training loss decreases significantly. These loss behaviours indicate that the models are unable to generalise the data and are overfitted. The gap between the training loss curve and the validation loss curve indicates the overfitting of the models and generalisation on the training data with both artifacts simultaneously.

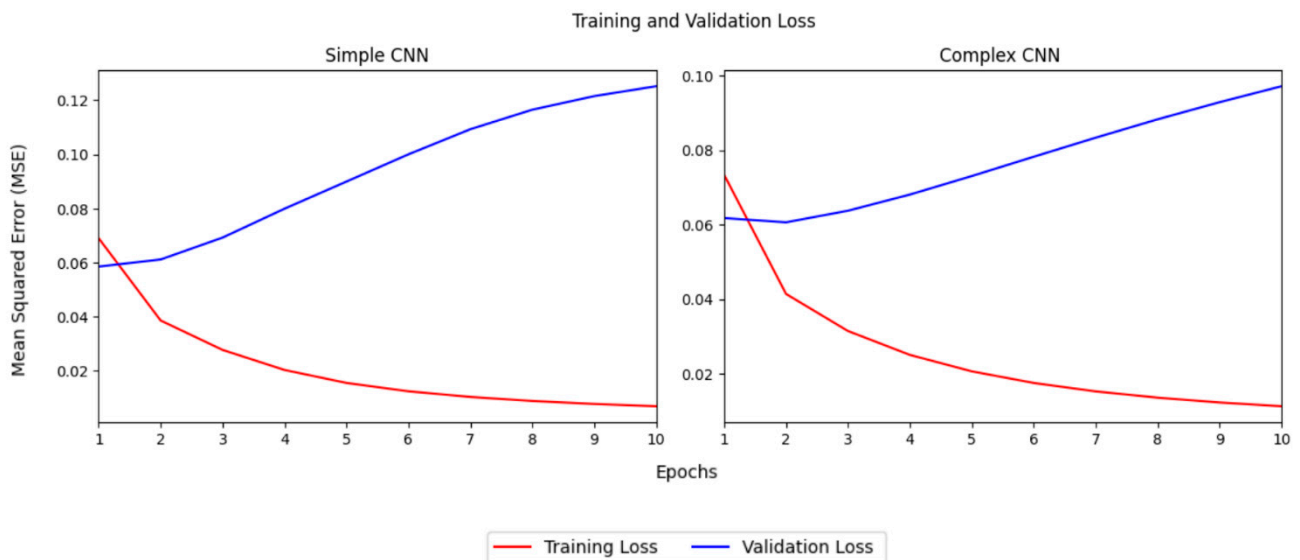


Figure 8. Training and validation loss curves for Complex CNN and Simple CNN.

The value for the training and validation losses are also higher for Simple CNN and Complex CNN as compared to the values for the proposed model. This indicates that the

proposed model performs better in capturing and learning the underlying features of the contaminated EEG signals than the other two networks.

4.3. Temporal and Spectral Evaluation of the Proposed Model

The performance of the proposed model was quantified on three evaluation metrics, i.e., $RRMSE(t)$, $RRMSE(f)$, and CC . The values of these parameters indicate the similarity between the ground-truth EEG signals and the denoised EEG signals obtained as the output from the model. The model was evaluated firstly by combining the EEG signal segments with the noise segments by assigning a value of SNR randomly. This was carried out to estimate the average performance of the model. The values of $RRMSE(t)$ and $RRMSE(f)$ were both found to be 0.35, while the CC value of the signals was calculated to be 0.94. The value of CC indicates a high similarity and a strong correlation between the ground-truth EEG signals and the denoised EEG signals. Moreover, the values of $RRMSE(t)$ and $RRMSE(f)$, show that the model's predictions are accurate to a great degree and have lesser room for error. This also shows the ability of the model to be equally effective at capturing the signal characteristics in both the time and the frequency domains.

As compared to the proposed model, the Simple CNN and the Complex CNN have higher values for the $RRMSE(t)$ and $RRMSE(f)$ and a smaller value of cross correlation between the denoised and the clean EEG signals. This difference in the values indicates that the proposed model effectively captures the subtle temporal and spectral properties of the noise present in the EEG signals and produces a denoised signal which greatly aligns with the clean EEG signal. The smaller values of the $RRMSE(t)$ and $RRMSE(f)$ shown in Table 1 also indicate that the proposed model can overcome the constraints of Simple CNN and Complex CNN. The higher cross correlation (CC) values of the proposed model demonstrate that the model is effectively able to remove the present artifacts in the EEG signal better than Simple CNN and Complex CNN.

Table 1. Evaluation metrics for combined artifact removal.

Model	$RRMSE(t)$	$RRMSE(f)$	CC
Complex CNN	0.56	0.56	0.85
Simple CNN	0.65	0.65	0.82
Proposed	0.35	0.35	0.94

Table 2 displays the power ratios of the frequency bands for the clean EEG signal, contaminated EEG signal, and the denoised EEG signals predicted from the proposed model. The power ratios across the frequency bands for the denoised EEG signal and the clean EEG signal are closely related numerically, which displays a high similarity between the signals.

Table 2. Power ratios for various frequency bands for denoised, EOG-EMG-contaminated, and clean EEG signals.

Frequency Band	Delta	Theta	Alpha	Beta	Gamma
Clean EEG Signal	0.383637	0.420987	0.104761	0.071334	0.019281
Denoised EEG Signal	0.376995	0.449792	0.097245	0.059614	0.016354
EOG-EMG-Contaminated EEG Signal	0.294029	0.187648	0.056777	0.101412	0.360134

The EOG artifacts lie in the Delta band while the EMG artifacts have high frequency components and exist in the Gamma band, as further visualised in Figure 9. The power ratio can be seen as having a high value in the Delta and Gamma bands because of the EOG and EMG artifacts. This can be seen to have been drastically reduced in the denoised EEG signal.

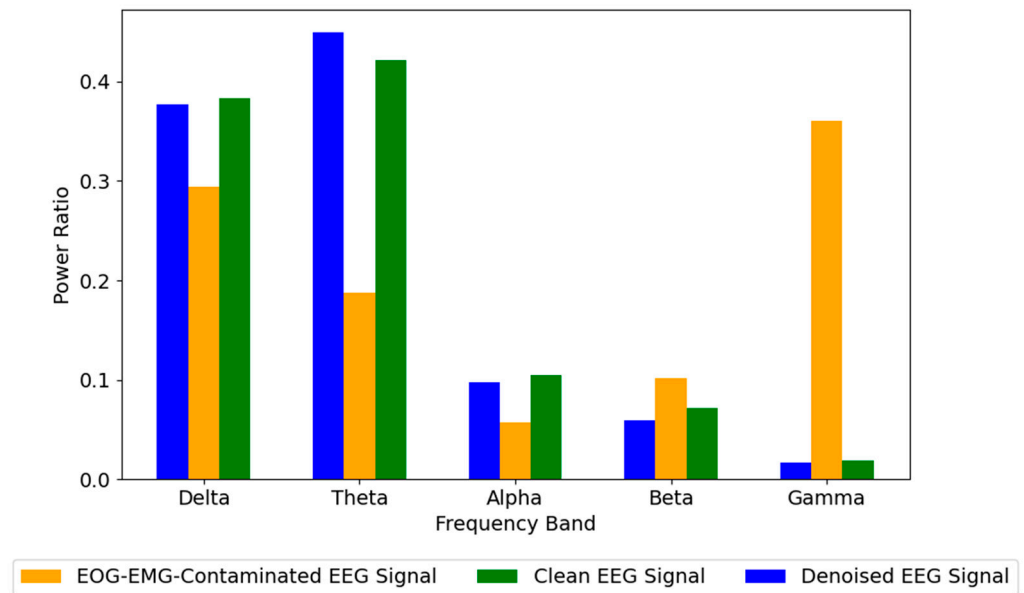


Figure 9. Power ratios for various frequency bands for denoised, EOG-EMG-contaminated, and clean EEG signals.

To observe the performance of the proposed model, the noisy EEG signal along with the ground-truth EEG signal and the denoised EEG signal were plotted in the time domain and spectral domain. Figure 10 displays the average performance of the proposed model in the time domain when the signal was contaminated with a range of SNR values to introduce randomness in noise behaviour. The denoised signal closely related to the clean EEG signal, which displays the robustness of the model in removing artifacts.

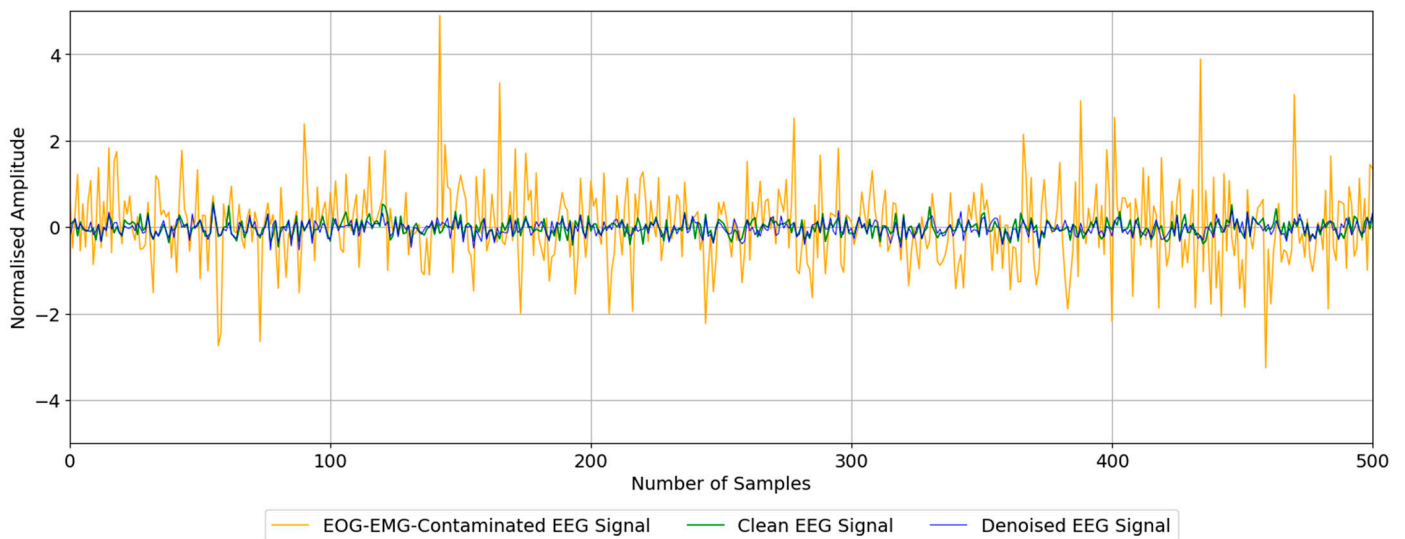


Figure 10. Temporal representation of denoised, EOG-EMG-contaminated, and clean EEG signals.

Figure 11 displays the model performance in the spectral domain. The high-frequency power in the contaminated signal appears to be reduced significantly in the denoised EEG signal while preserving the lower-frequency characteristics. This indicates a significant decrease in artifacts present in contaminated EEG signals without losing any of the main EEG characteristics.

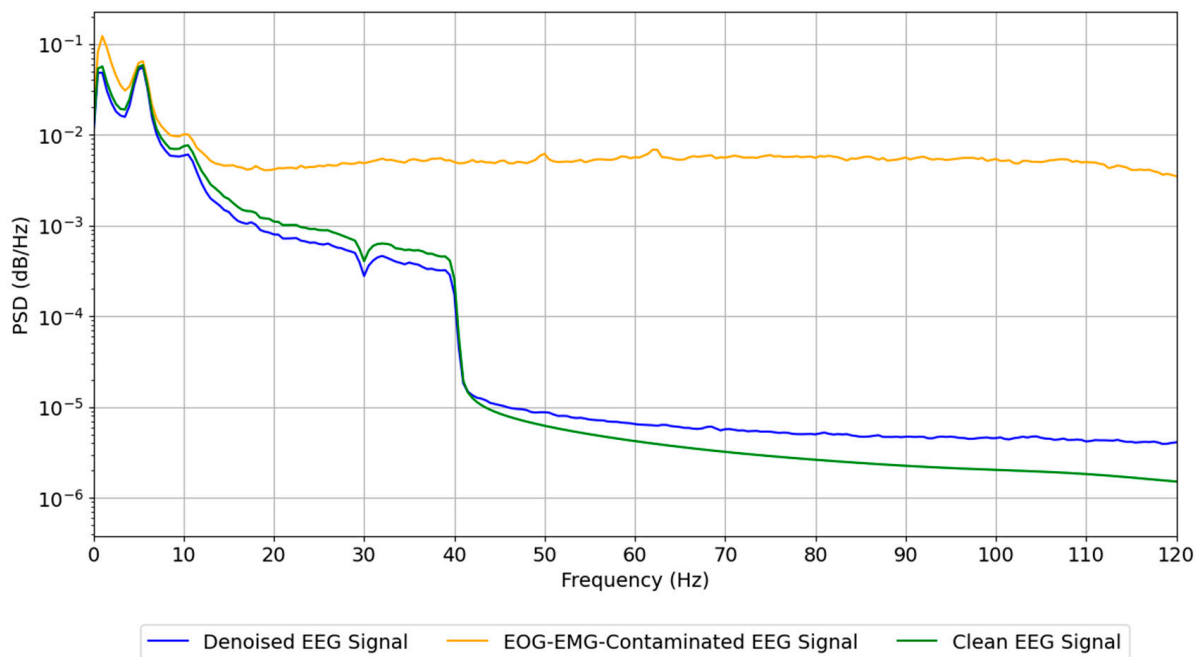


Figure 11. Spectral representation of denoised, EOG-EMG-contaminated, and clean EEG signals.

4.4. Evaluation on Different Signal-to-Noise Ratios

The proposed model was trained and evaluated on the training and testing data with specific signal-to-noise ratios (SNR) to observe the effect of varying noise on the model performance. The SNR value determined the amount of noise present in the training, validation, and testing data. The value of the SNR ranged from -7dB to $+2\text{dB}$. Table 3 displays and compares the values of $RRMSE(t)$, $RRMSE(f)$, and CC across the values of SNR values of -7dB to $+2\text{dB}$ with the contaminated EEG signal with both EOG and EMG artifacts simultaneously with the existing methods [50]. It can be observed from Table 3 that the proposed model performs exceptionally well overall but especially at lower values of the SNR. Multi-ResUNet3+ performs better than the proposed model at higher values of the SNR for $RRMSE(f)$ but not at the lower values of the SNR. The cross correlation is higher than those of the other models at all the values of the SNR, which further displays the effectiveness of the proposed model.

Table 3. A comparison of estimated performance metrics (CC , $RRMSE$ in time and frequency domains) across different SNR values.

Evaluation Metric	SNR (dB)	Model							
		Proposed Model	Complex CNN	Simple CNN	MultiResUNet3+ [50]	LinkNet [51]	MCGUNet [52]	UNet [23]	FPN [53]
$RRMSE(t)$	-7	0.677	1.033	1.0411	0.783	0.7989	0.7235	0.8122	0.8198
	-6	0.599	0.974	0.932	0.7446	0.7638	0.6873	0.7755	0.7758
	-5	0.543	0.869	0.839	0.6883	0.7088	0.6479	0.7189	0.7247
	-4	0.462	0.751	0.779	0.544	0.6532	0.5688	0.6524	0.6706
	-3	0.405	0.673	0.677	0.5675	0.5994	0.5222	0.6017	0.6108
	-2	0.374	0.557	0.555	0.5108	0.537	0.4476	0.5458	0.5438
	-1	0.357	0.480	0.468	0.448	0.4821	0.4526	0.4736	0.4871
	0	0.312	0.395	0.393	0.3821	0.4143	0.4054	0.4207	0.4338
	1	0.322	0.327	0.326	0.3375	0.361	0.4183	0.3603	0.3664
	2	0.266	0.274	0.278	0.2867	0.3107	0.3744	0.3118	0.3159

Table 3. Cont.

Evaluation Metric	SNR (dB)	Model							
		Proposed Model	Complex CNN	Simple CNN	MultiResUNet3+ [50]	LinkNet [51]	MCGUNet [52]	UNet [23]	FPN [53]
RRMSE(<i>f</i>)	-7	0.677	1.03	1.0411	0.7017	0.7447	0.6894	0.7903	0.8202
	-6	0.599	0.974	0.932	0.6587	0.7399	0.6364	0.7429	0.7842
	-5	0.543	0.869	0.839	0.5879	0.6578	0.569	0.7088	0.7222
	-4	0.462	0.751	0.779	0.4401	0.5969	0.4865	0.5999	0.6812
	-3	0.405	0.673	0.677	0.4768	0.5559	0.4545	0.5341	0.6136
	-2	0.374	0.557	0.555	0.4188	0.4972	0.3698	0.5027	0.5216
	-1	0.357	0.480	0.468	0.3577	0.4262	0.3625	0.4287	0.4701
	0	0.312	0.395	0.393	0.2934	0.3576	0.3196	0.3763	0.3945
	1	0.322	0.327	0.326	0.2542	0.3048	0.3374	0.3134	0.3289
2	0.266	0.274	0.278	0.2142	0.2622	0.2722	0.2635	0.2716	
CC	-7	0.758	0.620	0.618	0.6152	0.5987	0.663	0.5856	0.5771
	-6	0.807	0.654	0.670	0.6582	0.6512	0.7113	0.6355	0.637
	-5	0.849	0.705	0.719	0.7188	0.7052	0.7449	0.7039	0.6932
	-4	0.889	0.751	0.753	0.8191	0.7576	0.8009	0.7565	0.7507
	-3	0.915	0.804	0.802	0.8245	0.801	0.8388	0.8003	0.7982
	-2	0.928	0.856	0.858	0.858	0.8431	0.8819	0.8428	0.8423
	-1	0.934	0.889	0.895	0.8934	0.878	0.8832	0.8803	0.8757
	0	0.950	0.922	0.923	0.9228	0.9098	0.9094	0.9084	0.9025
	1	0.948	0.946	0.946	0.9411	0.9332	0.91	0.9325	0.9308
2	0.964	0.962	0.961	0.9579	0.9506	0.9277	0.9504	0.9496	

Similarly, Figures 12 and 13 also display the values for RRMSE (*t*), RRMSE (*f*), and CC plotted against the integer values of the SNR from -7dB to +2dB. The values for evaluations metrics are recorded for different values of the SNR to determine the effectiveness of the proposed model as compared to the other existing models when the amount of noise varies.

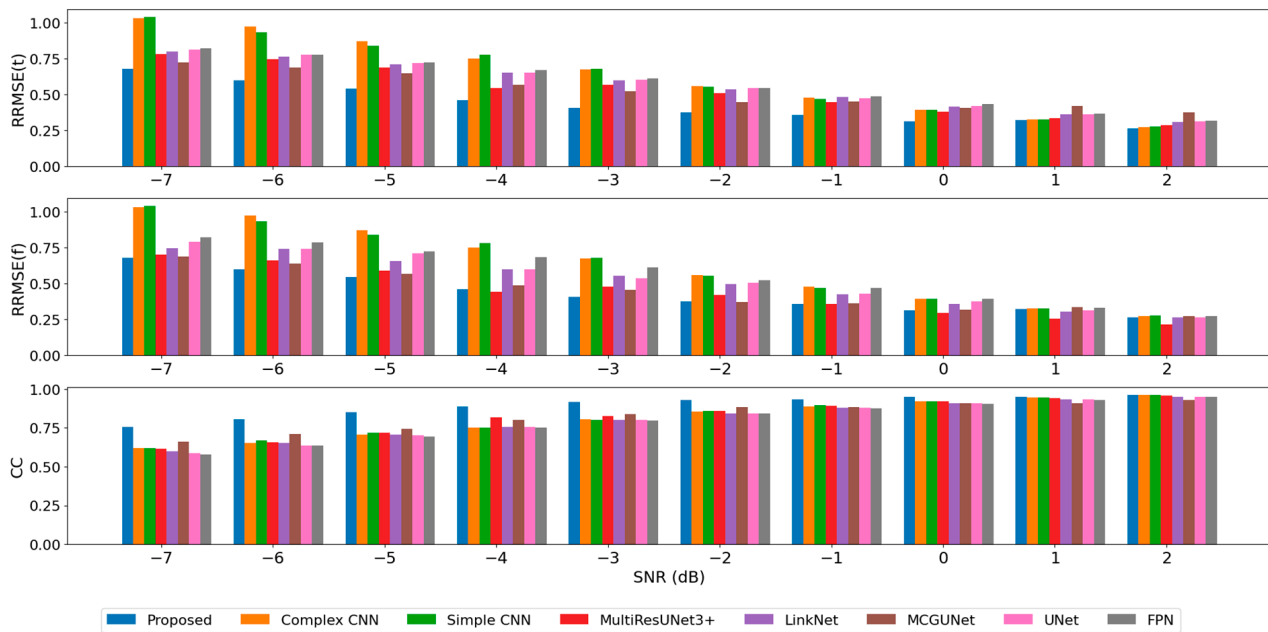


Figure 12. A comparison of estimated performance metrics (CC, RRMSE in time and frequency domains) across different SNR values.

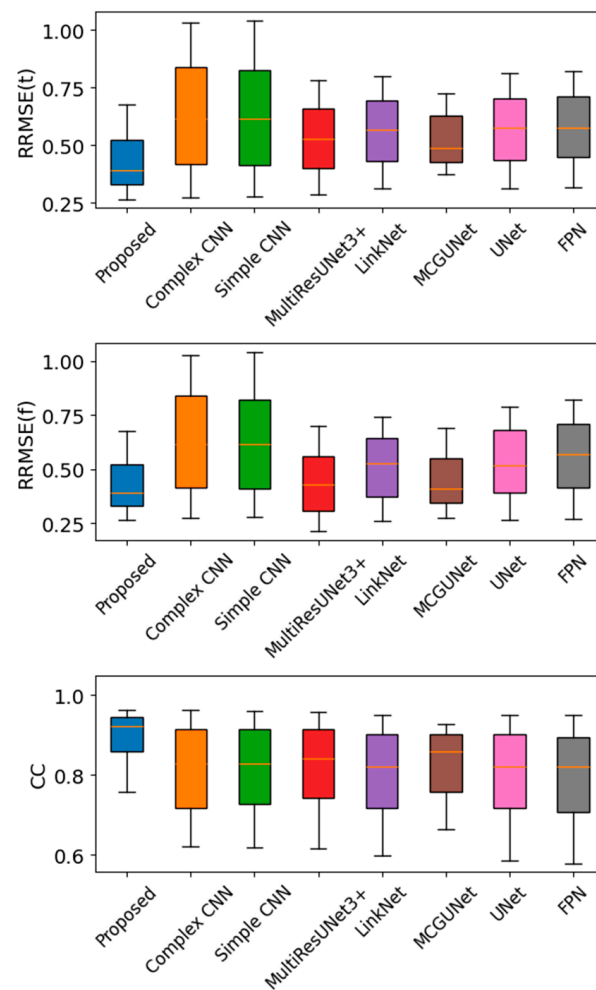


Figure 13. Comparison of performance between the proposed model and the existing models.

Table 3 lists the models' performances by calculating the values of $RRMSE$ in the time and frequency domains and CC between the denoised and clean EEG signals. The bold numerical values display the best performing model for each parameter and the SNR value. When the value of the SNR is low, i.e., the amount of noise present in the contaminated EEG signal is greater than the clean EEG signal, the proposed model performs exceptionally. The values of $RRMSE$ in both time and frequency domains are much lower than these values for the Complex CNN and Simple CNN. This indicates the better performance of the proposed model in removing artifacts from the contaminated EEG signals and producing denoised EEG signals as compared to the Complex CNN and Simple CNN.

However, when the value of the SNR starts to increase, the performance of the Simple CNN and Complex CNN improves greatly, and their performances are on par with the proposed model. The values for $RRMSE$ in both the time and frequency domains and CC for the proposed model are almost identical when the SNR is above +2dB, indicating the robustness and effectiveness of the proposed model.

The proposed model performs exceptionally better than the existing models, especially at low SNR values, for all three evaluation metrics. $RRMSE(t)$ remains consistently lower than the rest of the models for all values of the SNR between -7 dB and $+2$ dB. For values of the SNR higher than -1 dB, MultiResUNet3+ performs better than the proposed model. The proposed model, however, still performs comparatively better than the rest of the models on lower SNR values of -7 dB to -5 dB, proving its capability to remove artifacts when high noise is experienced. The cross correlation between the predicted signal and the clean EEG signal remains higher than the existing models throughout the range of values of the SNR .

Figure 12 graphically represents the trend in the values of $RRMSE(t)$, $RRMSE(f)$, and CC between the noisy EEG signals and the denoised EEG signals at various values of the signal-to-noise ratio across different models for the removal of the simultaneous EOG-EMG artifacts.

Figure 13 displays the spread of the values of the evaluation metrics for the proposed model and the existing models when the simultaneous EOG-EMG artifacts are removed. The values for the $RRMSE(t)$ and $RRMSE(f)$ are observed to be at the bottom of the plot while the cross correlations appear at the top of the plot.

5. Conclusions

The aim of this study is to denoise EEG signals by removing simultaneously occurring ocular and myogenic artifacts by employing a deep learning-based neural network. The denoising model is a convolutional neural network (CNN) architecture consisting of seven convolutional blocks, each having two 1D convolutional layers with a ReLU activation function, followed by an average pooling layer and a dropout layer, and a fully connected layer at the very end of the architecture. The convolutional blocks extract noise features from the contaminated EEG signal, while the fully connected layer reconstructs the denoised signal. Trained with the Adam optimiser, with batch sizes of 20 and 50 epochs, the model's effectiveness is evaluated using the mean squared error (MSE), the relative root mean square error in the time and frequency domains ($RRMSE(t)$ and $RRMSE(f)$), and cross-correlation (CC) coefficients. The low training and validation losses, alongside the close alignment between the $RRMSE$ and CC values, demonstrate the model's capability to accurately capture and denoise artifacts without overfitting. The model achieves $RRMSE$ values of 0.35 in the time and frequency domains and a CC value of 0.94, which indicates a strong alignment of the reconstructed EEG signals with clean EEG signals.

A comparative analysis shows that the proposed CNN model performs better than the existing models to remove simultaneously occurring EOG-EMG artifacts. The developed model exhibits lower training and validation losses, lower $RRMSE$ values in both the time and frequency domains, and higher cross-correlation (CC) coefficients than the benchmark models. Additionally, the proposed model has been proven to perform better than the existing models when evaluated across a range of signal-to-noise ratios (SNR) from -7 dB to $+2$ dB. It achieves significantly lower $RRMSE$ values and higher cross-correlation coefficients when compared with existing models in the literature, highlighting its ability to remove artifacts at different noise levels.

A limitation of this study is the absence of spatial convolution layers which restricts its capability to capture spatial patterns across different channels. This can result in ineffective performance in a multi-channel EEG configuration and effects the generalisability of the model. Moreover, the lack of phase-locked EOG and EMG data for model generalisation also limits the model's ability to learn the correlated noise patterns when the EOG and EMG signals occur in a synchronised pattern. A potential limitation of this study is the risk of data leakage, as often experienced by algorithms developed for medical applications, as the datasets available for model training are limited.

For future work, incorporating spatial convolutional layers in the existing model can widen the scope of the study. The existing model can be further enhanced to monitor and remove artifacts from real-time EEG signals effectively as well as to perform a study with correlated EOG and EMG signals. The model can also be evaluated using different validation methods and datasets to further enhance and explore its performance. It can also be enhanced to remove both physiological and non-physiological artifacts in a clinical setting.

Author Contributions: Conceptualization, M.A.; Methodology, M.A.; Software, M.A.; Validation, M.A.; Formal analysis, M.A.; Investigation, M.A.; Data curation, M.A.; Writing—original draft, M.A. and T.S.; Writing—review & editing, T.S. and A.A.; Supervision, T.S. and A.A. All authors have read and agreed to the published version of the manuscript.

Funding: This research received no external funding.

Data Availability Statement: The data and material used in this paper are appropriately referred to and described in this paper.

Conflicts of Interest: The authors declare no conflict of interest.

References

- Rahman, M.M.; Jahangir, M.Z.B.; Rahman, A.; Akter, M.; Nasim, M.D.A.A.; Gupta, K.D.; George, R. Breast Cancer Detection and Localizing the Mass Area Using Deep Learning. *Big Data Cogn. Comput.* **2024**, *8*, 80. [CrossRef]
- Volinsky-Fremont, S.; Horeweg, N.; Andani, S.; Barkey Wolf, J.; Lafarge, M.W.; de Kroon, C.D.; Ørtoft, G.; Høgdall, E.; Dijkstra, J.; Jobsen, J.J. Prediction of recurrence risk in endometrial cancer with multimodal deep learning. *Nat. Med.* **2024**, *30*, 1962–1973. [CrossRef] [PubMed]
- Khandakar, S. Unveiling Early Detection and Prevention of Cancer: Machine Learning And Deep Learning Approaches. *Educ. Adm. Theory Pract.* **2024**, *30*, 14614–14628. [CrossRef]
- Niehues, J.M.; Quirke, P.; West, N.P.; Grabsch, H.I.; van Treeck, M.; Schirris, Y.; Veldhuizen, G.P.; Hutchins, G.G.A.; Richman, S.D.; Foersch, S. Generalizable biomarker prediction from cancer pathology slides with self-supervised deep learning: A retrospective multi-centric study. *Cell Rep. Med.* **2023**, *4*, 100980. [CrossRef]
- Subramani, S.; Varshney, N.; Vijay Anand, M.; Soudagar, M.E.M.; Al-Keridis, L.A.; Upadhyay, T.K.; Alshammari, N.; Saeed, M.; Subramanian, K.; Anbarasu, K.; et al. Cardiovascular Diseases Prediction by Machine Learning Incorporation with Deep Learning. *Front. Med.* **2023**, *10*. [CrossRef]
- Ma, Z.; Hua, H.; You, C.; Ma, Z.; Guo, W.; Yang, X.; Qiu, S.; Zhao, N.; Zhang, Y.; Ho, D.; et al. FlexiPulse: A Machine-Learning-Enabled Flexible Pulse Sensor for Cardiovascular Disease Diagnostics. *Cell Rep. Phys. Sci.* **2023**, *4*, 101690. [CrossRef]
- Illakiya, T.; Karthik, R. Automatic detection of Alzheimer’s disease using deep learning models and neuro-imaging: Current trends and future perspectives. *Neuroinformatics* **2023**, *21*, 339–364.
- Dutta, A.K.; Raparathi, M.; Alsaadi, M.; Bhatt, M.W.; Dodda, S.B.; Sandhu, M.; Patni, J.C. Deep learning-based multi-head self-attention model for human epilepsy identification from EEG signal for biomedical traits. *Multimed. Tools Appl.* **2024**, *83*, 80201–80223. [CrossRef]
- Minopoulos, G.M.; Memos, V.A.; Stergiou, K.D.; Stergiou, C.L.; Psannis, K.E. A Medical Image Visualization Technique Assisted with AI-Based Haptic Feedback for Robotic Surgery and Healthcare. *Appl. Sci.* **2023**, *13*, 3592. [CrossRef]
- Goodman, E.D.; Patel, K.K.; Zhang, Y.; Locke, W.; Kennedy, C.J.; Mehrotra, R.; Ren, S.; Guan, M.; Zohar, O.; Downing, M. Analyzing surgical technique in diverse open surgical videos with multitask machine learning. *JAMA Surg.* **2024**, *159*, 185–192. [CrossRef]
- Kandel, E.R. *Principles of Neural Science*; McGraw-Hill Education: New York, NY, USA, 2021.
- Avitan, L.; Teicher, M.; Abeles, M. EEG Generator—A Model of Potentials in a Volume Conductor. *J. Neurophysiol.* **2009**, *102*, 3046–3059. [CrossRef] [PubMed]
- Jenke, R.; Peer, A.; Buss, M. Feature Extraction and Selection for Emotion Recognition from EEG. *IEEE Trans. Affect. Comput.* **2014**, *5*, 327–339. [CrossRef]
- Fink, A.; Grabner, R.H.; Benedek, M.; Reishofer, G.; Hauswirth, V.; Fally, M.; Neuper, C.; Ebner, F.; Neubauer, A.C. The creative brain: Investigation of brain activity during creative problem solving by means of EEG and fMRI. *Hum. Brain Mapp.* **2009**, *30*, 734–748. [CrossRef] [PubMed]
- Alhussein, M.; Muhammad, G.; Hossain, M.S. EEG Pathology Detection Based on Deep Learning. *IEEE Access* **2019**, *7*, 27781–27788. [CrossRef]
- Shaffer, M.A. Problem Record of the Month, No. 3: Asymmetrical Eye-Blink Artifact. *Am. J. EEG Technol.* **1970**, *10*, 153–156. [CrossRef]
- Sweeney, K.T.; Ward, T.E.; McLoone, S.F. Artifact Removal in Physiological Signals—Practices and Possibilities. *IEEE Trans. Inf. Technol. Biomed.* **2012**, *16*, 488–500. [CrossRef]
- Bos, D.P.-O. Automated Artifact Detection in BrainStream An Evaluation of An Online Eye and Muscle Artifact Detection Method. 2008. Available online: <https://api.semanticscholar.org/CorpusID:13841013> (accessed on 1 August 2024).
- Kang, J.-S.; Ojha, A.; Lee, G.; Lee, M. Difference in brain activation patterns of individuals with high and low intelligence in linguistic and visuo-spatial tasks: An EEG study. *Intelligence* **2017**, *61*, 47–55. [CrossRef]
- Chen, Y.; Zhao, Q.; Hu, B.; Li, J.; Jiang, H.; Lin, W.; Li, Y.; Zhou, S.; Peng, H. A method of removing Ocular Artifacts from EEG using Discrete Wavelet Transform and Kalman Filtering. In Proceedings of the 2016 IEEE International Conference on Bioinformatics and Biomedicine (BIBM), Shenzhen, China, 15–18 December 2016. [CrossRef]
- Yin, J.; Liu, A.; Li, C.; Qian, R.; Chen, X. Frequency Information Enhanced Deep EEG Denoising Network for Ocular Artifact Removal. *IEEE Sens. J.* **2022**, *22*, 21855–21865. [CrossRef]
- Mashhadi, N.; Zargari, A.; Heidari, M.; Khaledyan, D. Deep learning denoising for EOG artifacts removal from EEG signals. In Proceedings of the 2020 IEEE Global Humanitarian Technology Conference (GHTC), Seattle, WA, USA, 29 October–1 November 2020. [CrossRef]

23. Ronneberger, O.; Fischer, P.; Brox, T. U-Net: Convolutional Networks for Biomedical Image Segmentation. In *Medical Image Computing and Computer-Assisted Intervention—MICCAI 2015*; Navab, N., Hornegger, J., Wells, W.M., Frangi, A.F., Eds.; Springer International Publishing: Munich, Germany, 2015; pp. 234–241.
24. Zhang, H.; Zhao, M.; Wei, C.; Mantini, D.; Li, Z.; Liu, Q. EEGdenoiseNet: A benchmark dataset for deep learning solutions of EEG denoising. *J. Neural Eng.* **2021**, *18*, 056057. [[CrossRef](#)]
25. Comon, P. Independent component analysis, A new concept? *Signal Process.* **1994**, *36*, 287–314. [[CrossRef](#)]
26. Delorme, A.; Makeig, S. EEGLAB: An open source toolbox for analysis of single-trial EEG dynamics including independent component analysis. *J. Neurosci. Methods* **2004**, *134*, 9–21. [[CrossRef](#)] [[PubMed](#)]
27. Gauba, H.; Kumar, P.; Roy, P.P.; Singh, P.; Dogra, D.P.; Raman, B. Prediction of advertisement preference by fusing EEG response and sentiment analysis. *Neural Netw.* **2017**, *92*, 77–88. [[CrossRef](#)]
28. Harender; Sharma, R.K. EEG signal denoising based on wavelet transform. In Proceedings of the 2017 International Conference of Electronics, Communication and Aerospace Technology (ICECA), Coimbatore, India, 20–22 April 2017; Volume 1, pp. 758–761. [[CrossRef](#)]
29. Al-Qazzaz, N.; Hamid Bin Mohd Ali, S.; Ahmad, S.; Islam, M.; Escudero, J. Automatic Artifact Removal in EEG of Normal and Demented Individuals Using ICA–WT during Working Memory Tasks. *Sensors* **2017**, *17*, 1326. [[CrossRef](#)] [[PubMed](#)]
30. Correa, A.G.; Laciari, E.; Patiño, H.D.; Valentinuzzi, M.E. Artifact removal from EEG signals using adaptive filters in cascade. *J. Phys. Conf. Ser.* **2007**, *90*, 012081. [[CrossRef](#)]
31. Shahabi, H.; Moghimi, S.; Zamiri-Jafarian, H. EEG eye blink artifact removal by EOG modeling and Kalman filter. In Proceedings of the 2012 5th International Conference on BioMedical Engineering and Informatics, Chongqing, China, 16–18 October 2012; pp. 496–500. [[CrossRef](#)]
32. Somers, B.; Francart, T.; Bertrand, A. A generic EEG artifact removal algorithm based on the multi-channel Wiener filter. *J. Neural Eng.* **2018**, *15*, 036007. [[CrossRef](#)]
33. van Driel, J.; Olivers, C.N.L.; Fahrenfort, J.J. High-pass filtering artifacts in multivariate classification of neural time series data. *J. Neurosci. Methods* **2021**, *352*, 109080. [[CrossRef](#)]
34. Gong, S.; Zhang, X.; Nguyen, X.A.; Shi, Q.; Lin, F.; Chauhan, S.; Ge, Z.; Cheng, W. Hierarchically resistive skins as specific and multimetric on-throat wearable biosensors. *Nat. Nanotechnol.* **2023**, *18*, 889–897. [[CrossRef](#)]
35. Hossain, M.S.; Reaz, M.B.I.; Chowdhury, M.E.H.; Ali, S.H.M.; Bakar, A.A.A.; Kiranyaz, S.; Khandakar, A.; Alhatou, M.; Habib, R. Motion Artifacts Correction From EEG and fNIRS Signals Using Novel Multiresolution Analysis. *IEEE Access* **2022**, *10*, 29760–29777. [[CrossRef](#)]
36. Wang, G.; Teng, C.; Li, K.; Zhang, Z.; Yan, X. The Removal of EOG Artifacts From EEG Signals Using Independent Component Analysis and Multivariate Empirical Mode Decomposition. *IEEE J. Biomed. Health Inform.* **2016**, *20*, 1301–1308. [[CrossRef](#)]
37. Marino, M.; Liu, Q.; Koudelka, V.; Porcaro, C.; Hlinka, J.; Wenderoth, N.; Mantini, D. Adaptive optimal basis set for BCG artifact removal in simultaneous EEG-fMRI. *Sci. Rep.* **2018**, *8*, 8902. [[CrossRef](#)] [[PubMed](#)]
38. De Clercq, W.; Vergult, A.; Vanrumste, B.; Van Paesschen, W.; Van Huffel, S. Canonical Correlation Analysis Applied to Remove Muscle Artifacts From the Electroencephalogram. *IEEE Trans. Biomed. Eng.* **2006**, *53*, 2583–2587. [[CrossRef](#)] [[PubMed](#)]
39. Chen, X.; Chen, Q.; Zhang, Y.; Wang, Z.J. A Novel EEMD-CCA Approach to Removing Muscle Artifacts for Pervasive EEG. *IEEE Sens. J.* **2019**, *19*, 8420–8431. [[CrossRef](#)]
40. Luo, T.; Fan, Y.; Chen, L.; Guo, G.; Zhou, C. EEG Signal Reconstruction Using a Generative Adversarial Network With Wasserstein Distance and Temporal-Spatial-Frequency Loss. *Front. Neuroinformatics* **2020**, *14*, 15. [[CrossRef](#)] [[PubMed](#)]
41. Fahimi, F.; Dosen, S.; Ang, K.K.; Mrachacz-Kersting, N.; Guan, C. Generative Adversarial Networks-Based Data Augmentation for Brain–Computer Interface. *IEEE Trans. Neural Netw. Learn. Syst.* **2021**, *32*, 4039–4051. [[CrossRef](#)]
42. Sawangjai, P.; Trakulruangroj, M.; Boonnag, C.; Piriyaajakonkij, M.; Tripathy, R.K.; Sudhawiyangkul, T.; Wilaiprasitporn, T. EEGANet: Removal of Ocular Artifacts From the EEG Signal Using Generative Adversarial Networks. *IEEE J. Biomed. Health Inform.* **2022**, *26*, 4913–4924. [[CrossRef](#)]
43. Zhang, H.; Wei, C.; Zhao, M.; Liu, Q.; Wu, H. A Novel Convolutional Neural Network Model to Remove Muscle Artifacts from EEG. In Proceedings of the ICASSP 2021—2021 IEEE International Conference on Acoustics, Speech and Signal Processing (ICASSP), Toronto, ON, Canada, 6–11 June 2021; pp. 1265–1269. [[CrossRef](#)]
44. Zhang, Z.; Yu, X.; Rong, X.; Iwata, M. A Novel Multimodule Neural Network for EEG Denoising. *IEEE Access* **2022**, *10*, 49528–49541. [[CrossRef](#)]
45. Sun, W.; Su, Y.; Wu, X.; Wu, X. A novel end-to-end 1D-ResCNN model to remove artifact from EEG signals. *Neurocomputing* **2020**, *404*, 108–121. [[CrossRef](#)]
46. Yang, B.; Duan, K.; Zhang, T. Removal of EOG artifacts from EEG using a cascade of sparse autoencoder and recursive least squares adaptive filter. *Neurocomputing* **2016**, *214*, 1053–1060. [[CrossRef](#)]
47. Wang, B.; Deng, F.; Jiang, P. EEGDiR: Electroencephalogram denoising network for temporal information storage and global modeling through Retentive Network. *Comput. Biol. Med.* **2024**, *177*, 108626. [[CrossRef](#)]
48. Saha, P.; Ansaruddin Kunju, A.K.; Majid, M.E.; Bin Abul Kashem, S.; Nashbat, M.; Ashraf, A.; Hasan, M.; Khandakar, A.; Shafayet Hossain, M.; Alqahtani, A.; et al. Novel multimodal emotion detection method using Electroencephalogram and Electrocardiogram signals. *Biomed. Signal Process. Control* **2024**, *92*, 106002. [[CrossRef](#)]

49. Qu, H.; Fan, Z.; Cao, S.; Pang, L.; Wang, H.; Zhang, J. A Study on Sensitive Bands of EEG Data under Different Mental Workloads. *Algorithms* **2019**, *12*, 145. [[CrossRef](#)]
50. Hossain, M.S.; Mahmud, S.; Khandakar, A.; Al-Emadi, N.; Chowdhury, F.A.; Mahbub, Z.B.; Reaz, M.B.I.; Chowdhury, M.E.H. MultiResUNet3+: A Full-Scale Connected Multi-Residual UNet Model to Denoise Electrooculogram and Electromyogram Artifacts from Corrupted Electroencephalogram Signals. *Bioengineering* **2023**, *10*, 579. [[CrossRef](#)] [[PubMed](#)]
51. Chaurasia, A.; Culurciello, E. LinkNet: Exploiting encoder representations for efficient semantic segmentation. In Proceedings of the 2017 IEEE Visual Communications and Image Processing (VCIP), St. Petersburg, FL, USA, 10–13 December 2017; pp. 1–4. [[CrossRef](#)]
52. Asadi-Aghbolaghi, M.; Azad, R.; Fathy, M.; Escalera, S. Multi-level Context Gating of Embedded Collective Knowledge for Medical Image Segmentation. *arXiv* **2020**, arXiv:2003.05056. [[CrossRef](#)]
53. Lin, T.-Y.; Dollár, P.; Girshick, R.; He, K.; Hariharan, B.; Belongie, S. Feature Pyramid Networks for Object Detection. In Proceedings of the 2017 IEEE Conference on Computer Vision and Pattern Recognition (CVPR), Honolulu, HI, USA, 21–26 July 2017; pp. 936–944. [[CrossRef](#)]

Disclaimer/Publisher’s Note: The statements, opinions and data contained in all publications are solely those of the individual author(s) and contributor(s) and not of MDPI and/or the editor(s). MDPI and/or the editor(s) disclaim responsibility for any injury to people or property resulting from any ideas, methods, instructions or products referred to in the content.